Reactions of halogens with surfaces stimulated by VUV light

Verena Ney and Nikolaus Schwentner

Institut für Experimentalphysik, Freie Universität Berlin, Arnimallee 14, D-14195 Berlin, Germany

E-mail: nikolaus.schwentner@physik.fu-berlin.de

Abstract

Reactions of halogens (Cl_2, XeF_2) with metals (Cu) and semiconductors (Si, GaAs) are investigated. The main focus is put on light induced reactions, stimulated by synchrotron radiation in the spectral range from 200 to 50 nm, in comparison with the dark reaction. Growth of reaction products on the surface and the desorption of volatile compounds are studied. A set-up with a quartz microbalance was adopted to determine reaction rates *in situ*. The rates are very sensitive to sample preparation. In the system Cu/Cl_2, oxygen was found to especially slow down the reaction and much higher reaction rates than reported previously were observed for pure samples. Measurements with masks show the possibility of using desorption (also called light induced dry etching) to microstructure materials. Analysis of the irradiations with different wavelengths reveals a high spectral dependence of the reactions, which can therefore be controlled. The efficiency of the light induced non-selective reaction follows the gas phase absorption of the etching gases, whereas selective reactions, which are used to structure the materials, are induced in adsorbed halogens at different wavelengths. High efficiencies of single-photon events, due to chain reactions, with multiplication factors of the order of 10^5, are observed. The resulting pit size has to be contrasted with the intended spatial resolution.

1. Introduction

Reactions on surfaces have remained a fascinating field of research for decades and new facets of this subject are developing at a fast pace. Following the reaction dynamics with ultrashort spectroscopy [1, 2], triggering reactions with high spatial resolution in STMs [3] and combining these tools, in the near future [4], will provide access to an unprecedentedly detailed experimental characterization. Stimulation with light delivers the energy to drive the reaction and it sets the time triggering required to follow the time course. Thus the deposition of photon energy, its migration, the initiation of a bunch of reactions and the final branching

into different kinds of reactions, of which desorption is the most original one for surfaces, will remain basic ingredients [5]. Surprises are guaranteed, as recent observations of phonon pile-up leading to electronic excitation and desorption show [6]. Obviously there is still a real challenge in revealing the basic chemical and photochemical elementary processes involved in surface reactions. In addition there is a strong requirement for structuring surfaces with increased spatial resolution [7]. Localized desorption is a natural route for converting a light pattern on a surface into a permanent structural pattern. Besides the near field methods which are *en vogue* for generating high spatial resolutions, the far field techniques have their specific merits as regards generality and throughput. To improve their resolution it is necessary to resort to shorter wavelengths, as displayed for example in the International Technology Roadmap for Semiconductors[1]. This shifts the emphasis from 193 nm wavelength further into the VUV spectral region, to 157 nm and even to 13.5 nm in the EUV project.

In this contribution, investigations on light induced surface reactions in the spectral range from 200 to 50 nm which have been carried out in our group are summarized. An appropriate light source is synchrotron radiation as regards tunability and stability. To achieve a sufficient photon flux has remained however a challenge, ever since the first patterning experiments carried out on beamlines in Japan [8, 9]. We have increased the photon flux from bending magnets by introducing mirrors collecting a large angular range [10] at the 3m-NIM-2 beamline at BESSY I as well as in the continuation at the 3m-NIM-1 beamline at BESSY II. Halogen molecules like Cl_2, F_2 and XeF_2 are used as reagents. They are rather reactive already in the ground state. In addition they have strong electronic transitions in the spectral range from 150 to 50 nm and it is expected that the reactivity can be enhanced further by stimulating these excited states with light. The reactions are induced on Cu plates [11–15] and films [16] and on single-crystalline Si(100) [17–23] and GaAs(100) [24–27] surfaces in order to cover relevant metallic and semiconductor systems. Due to the high reactivity of halogens it is necessary in a first step to separate the reaction of ground state atoms, which is independent from irradiation and therefore called dark reaction, from the light induced reactions. In a second step, conditions for a dominance of the light induced reaction have to be established.

An exemplary study has been carried out for Cu and Cl_2 since they have the strongest dark reactions among the systems considered [15]. In addition, the reaction products are the stable CuCl and $CuCl_2$ compounds. Therefore the accumulation of these products and their composition can be followed and analysed in relation to exposure time. Typically the products are investigated in a stepwise series of irradiation intervals. Here we present the adoption of an instrument which is very successfully applied in related areas, i.e. the quartz microbalance, to follow the development of light induced reactions with synchrotron radiation [28]. It turns out that the stability and the sensitivity requirements are very demanding. However, now a continuous recording of the mass deposition in the reaction is possible. Indeed these new results correct previous conclusions concerning the dark reaction. As a consequence, modifications are derived which are necessary to slow down this dark reaction in order to favour the light induced one for the available photon flux.

The difficulties in directly recording the mass changes at incubation rates of typically 10^{12} atoms s^{-1} are rather easily overcome by accumulation of typical time steps of 10^3 s and investigating the spatial patterns of product films formed on the surface via irradiation with masks. In this way the wavelength dependence of the quantum efficiencies of the reactions will be deduced.

As regards the quantum efficiency, the directly determined quantum efficiency q_1 of compounds formed per number of photons incident in the reaction cell and the quantum

---

[1] The International Roadmap for Semiconductors 2004, update Lithography, figure 53.

efficiency q_2 of compounds formed per number of photons absorbed in the reactive medium have to be distinguished [23]. q_1 is more relevant for application purposes in terms of overall efficiency of a photon and thus throughput and requirements for the light sources. q_2 provides insight into the elementary reaction processes which are initiated by the photon on a molecular level.

The results for the basic Cu and Cl_2 system reveal two very distinct classes of light induced processes which are called selective and non-selective respectively. A reaction cell consists of the substrate (metal, semiconductor) which is irradiated through the halogen gas in front of it. A photon can be absorbed in a reactive surface layer (or in the bulk). In this case the reaction is started in the laterally well defined spot of absorption and this reaction is called selective. If a photon is absorbed in the halogen gas, then diffusion of the excited species, until it reaches the surface and starts a reaction, will lead to a lateral displacement and the reaction is called non-selective. A lateral modulation of the light intensity for example from the structure of a mask will be reproduced in the lateral distribution of reaction products on the surface in the selective case and it will be washed out in the non-selective case [23].

Obviously selective processes have to be targeted for direct structuring with photochemical surface processes. This will be demonstrated for the halogen/semiconductor systems. Combinations have been chosen for which several compounds from the reaction are volatile. In this case light induced desorption, the central topic here, occurs and substrate material is removed with these volatile compounds. Thus direct reproduction of mask structures on a semiconductor surface becomes feasible via this so called light induced dry etching. Inspection of the dependence on halogen pressure and wavelength reveals that a rich variety of passivation, dissociation and migration processes are involved.

As regards an efficient use of photons it turns out that the q_2 efficiencies are indeed very high and even exceed unity. This provides an immediate proof that the reaction extends beyond a single molecule and the underlying amplification processes still await an explanation. The local expansion of the pit from a single-photon event due to this amplification will be directly displayed. Consequences as regards the optimal balance between a desired high efficiency for being cost effective and a degradation of the spatial resolution due to the pit size will be addressed finally.

2. Online measurement of reaction rates with a quartz microbalance

2.1. Adoption of a quartz microbalance for a reaction cell and a synchrotron radiation set-up

A quartz microbalance is a well established and robust device for recording *in situ* mass changes due to intake or desorption of reaction products [29, 30]. It is compatible with UHV requirements in open beam experiments with synchrotron radiation. It can withstand the chemically aggressive halogen atmosphere in the reaction cell and appropriate electric contacting is feasible. A sensitivity limit of 0.5% of a monolayer per minute has been achieved for optimal environment conditions in a laboratory [31], and frequency changes of 0.04 Hz min^{-1} are significantly above the noise level. A synchrotron laboratory has an increased background of electronic noise and thermal stability is especially a problem. We used a crystal with an AT cut to reduce the thermal sensitivity. Nevertheless, the periodic change of the temperature at BESSY II following the day–night cycles caused a drift of typically 0.05 Hz min^{-1} of the crystal frequency with a change of sign from day to night according to a two-week survey shown in figure 1(a).
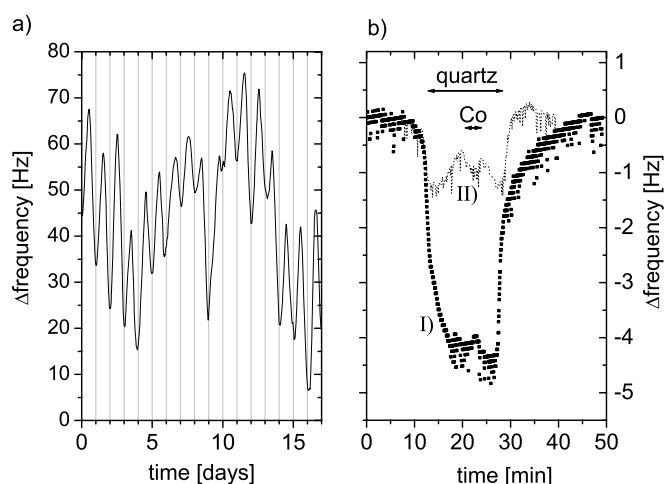
Figure 1. (a) Due to the thermal sensitivity of the quartz microbalance the frequency changes in the course of a two-week observation with a period of a day. (b) Scanning the zeroth order across the quartz induces a temperature change, which is observed via the frequency change. Quartz II has good thermal contact to the sample holder, whereas quartz I has a bad one and is therefore much more sensitive to irradiation.

The frequency change Δf for a mass change Δm according to [32]

$$\frac{\Delta f}{f} = -\frac{\Delta m}{m} = -\frac{\Delta m}{\rho \cdot A \cdot d} \tag{1}$$

corresponds for the used crystals with eigenfrequency $f = 6$ MHz, density $\rho = 2.65$ g cm^{-3}, area $A = 1.49$ cm^2 and thickness $d = 0.278$ mm to a frequency change $\Delta f = 3.23 \times 10^{-15}$ Hz for addition of a single Cl atom with $\Delta m = 59.3 \times 10^{-24}$ g. The achievable flux of photons γ at the beamline 3m-NIM-1 at BESSY II is of the order of $6 \times 10^{13} \gamma$ min^{-1} on the crystal and will be detailed later on. An optimistic estimate of $q_1 = 1$, meaning that every photon impinging on the cell initiates a reaction which leads to an intake of Cl atoms from the etching gas with an efficiency of unity, leads to a rate of $\Delta f(t) = 0.2$ Hz min^{-1}. Obviously it is necessary to optimize flux and efficiency in order to compete with the background effects. In addition, it is necessary to accumulate $\Delta f(t)$ for at least several minutes before changing external parameters like wavelength and gas pressure.

Evaporated films on the quartz crystal are necessary for the method and the purity of the Cu films is crucial, as will be pointed out later. Therefore *in situ* preparation and a separation from the etching gas is indispensable. The Cu wire pieces are evaporated from a Mo crucible with an electron beam evaporator (Omicron EFM 3) in UHV in the upper chamber sketched in figure 2(a) and condensed through a mask onto the quartz crystal. The Cu film thickness is derived from the frequency change of the crystal. The crystal holder is transferred by a wobble stick m_1 through the gate valve V to the main chamber and is taken up by a second manipulator m_2. Figure 2(b) illustrates the positioning of the holder on m_2 by a small magnet M and the closing of the electrical contact for the quartz crystal. Finally the holder is moved horizontally to seal the back of the reaction cell. The flow of etching gas is maintained by two tubes and stabilized in a range of 0.3–10 sccm by a mass flow controller (Aera FC–D980C). A halogen/inert gas mixture is contained in another UHV compatible gas reservoir.

The front of the etching cell is covered with an MgF$_2$ window for these measurements; it has a cut-off wavelength of 113 nm. The whole set-up is placed at an exit arm of the 3m-NIM-1
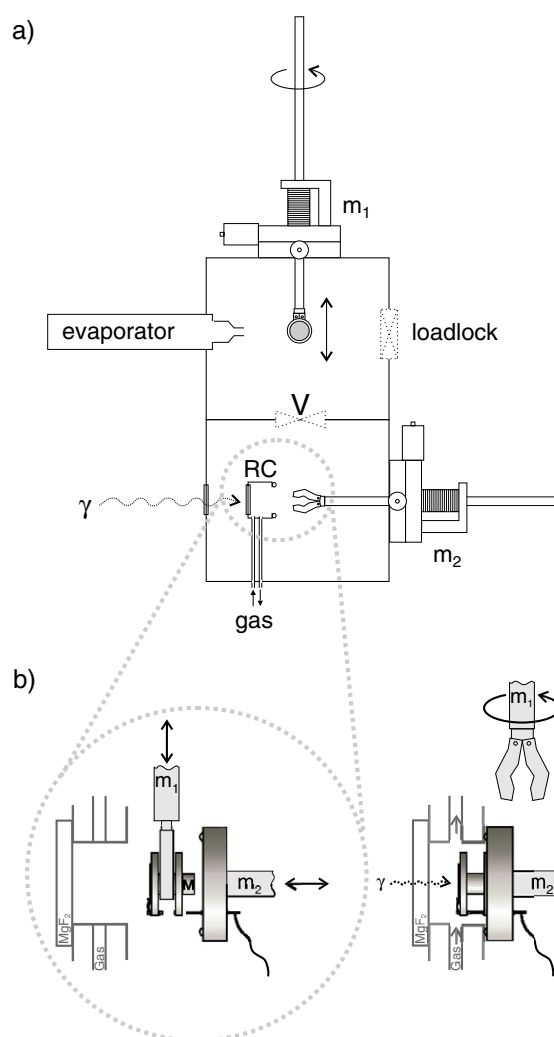
Figure 2. Set-up for *in situ* preparation of films which are exposed to gas and irradiated in the reaction cell RC. (a) Preparation position in front of the evaporator. After preparation the sample is transferred with manipulators m_1 and m_2 into the reaction cell. (b) A little magnet M holds the sample, which is positioned in the reaction cell with m_2. The cell is also closed with m_2.

monochromator in such a way that the focal spot coincides with the centre of the quartz crystal as sketched in figure 3. In the zeroth order of the grating (figure 4(a)) undispersed white light is concentrated in a small central spot of about 1.3 mm width and 0.3 mm height. In first order the spectrum is dispersed vertically across the crystal as indicated in figure 4(b). The stripe is 1.3 mm wide and for the grating used with 600 lines mm^{-1} the wavelength dispersion in the vertical direction is 0.6 nm mm^{-1}.

2.2. Sample preparation and alignment

The quartz crystals with $d_3 = 13.8$ mm diameter were coated by the delivering company (Quarztech) with gold. The copper was deposited with a much smaller diameter of $d_2 =$
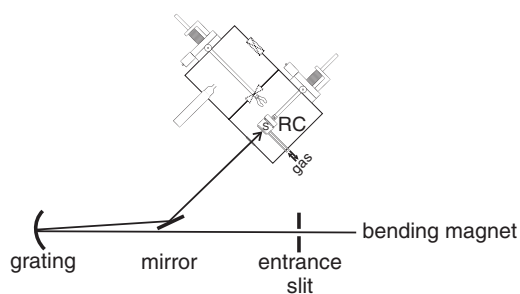
Figure 3. Scheme of monochromator (3m-NIM-1, BESSY II) with etching set-up. Dispersed light is focused via the grating on the sample S, in the reaction cell RC.
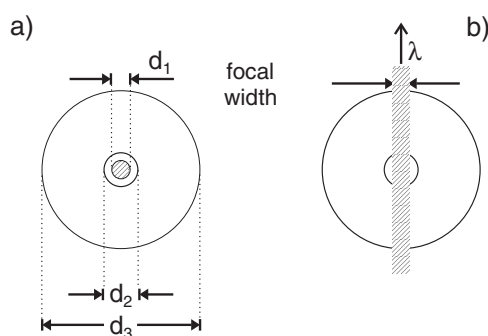

Figure 4. (a) Quartz substrate (diameter d_3) with sample material (d_2) and the irradiated spot in zeroth order (d_1). (b) Irradiated stripe with dispersed light showing central wavelength λ.

2.85 mm in most cases. The dark reaction will attack the area characterized by d_2 while the light induced reaction is restricted to the width d_1. In order to enhance the ratio of light induced to dark contributions we have chosen d_2 close to d_1 with a margin for tolerating alignment errors. The effective surface area increases with roughness which supports the dark reaction. The as-fabricated sawn quartz crystals have a very rough surface and therefore we used crystals which were polished and then covered with gold. The improvement in smoothness is demonstrated in the AFM pictures of figure 5 where the greyscale from (a) to (d) was increased systematically to enlarge sensitivity. The unpolished crystal in (a) has a roughness amplitude of 1.3 μm, which is reduced by polishing to 90 nm (b). Gold deposition furthermore flattens to 49 nm (c) and addition of the Cu film leads to maximal amplitudes of 34 nm. The gold film shows islands with typically 10 nm height and 150 nm diameter which seem to be covered homogeneously by the Cu film.

It turned out that the reactions are especially sensitive to spurious contaminations of the Cu film with oxygen. Therefore the results are grouped into those for clean Cu abbreviated as Cu(pure) and those for oxygen contaminated Cu abbreviated as Cu(O).

Cu wire pieces of 99.95% specified purity were melted in a crucible and tempered. The higher melting temperature of the oxides with respect to pure Cu prevents sufficient oxide evaporation in the tempering procedure. For Cu(pure) samples the oxygen coverage on the wire surface was removed mechanically before filling the crucible, the highest evaporation rates were used to avoid contamination from residual gas and the samples were immediately transferred and etched. Any one of the following changes originated in a Cu(O) behaviour in
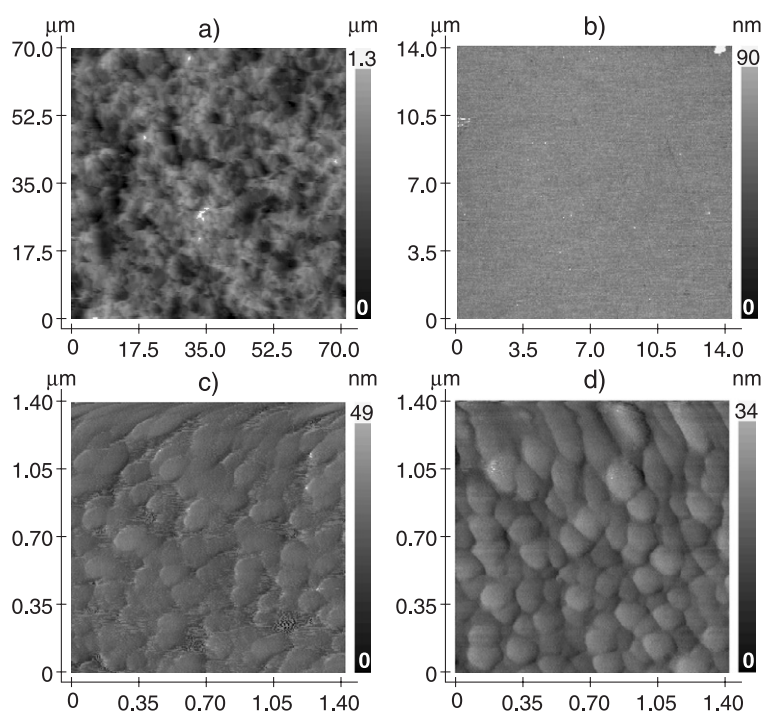
Figure 5. AFM pictures of quartz surfaces. (a) Unpolished quartz with 1.3 μm roughness. (b) Overview of the polished quartz substrate, 90 nm roughness. (c) Enhancing the resolution further (scanning a smaller area) shows that the surface is covered with isles of gold. (d) After evaporating Cu onto the quartz, the isles are still observed.

the etching procedure: use of Cu wire with original oxygen coverage, slow deposition rate, delay in transfer and etching or even exposure of a film to atmosphere.

Irradiation of the quartz crystal with a large photon flux in zeroth order leads to heating which is visible in frequency changes. Typical changes for light on/light off in an empty etching cell of 1–2 Hz are reduced in a gas filled cell to 0.5 Hz due to additional cooling. The effect can be enhanced by a weak thermal contact of the quartz to the substrate (I) in figure 1(b) and it can be used for control of alignment. The light beam is scanned across the crystal in figure 1(b) where the frequency decrease and recovery mark the crystal boundaries. The structure in the plateau reflects the central reactive spot. Thermal equilibrium is reached slowly for the weakly coupled crystal (I) and the flanks are smeared out with respect to the abrupt ones of the well coupled one (II). Motion of the light spot in the 0.1–1 mm regime can occur in wavelength tuning due to lateral angular motion of the grating and it is detrimental because fresh and pre-irradiated areas are interchanged in an uncontrolled way. Checks analogous to that of figure 1(b) reveal such effects [16].

2.3. Dark reaction of Cu(pure)

A systematic investigation of the reaction rate $k(t)$ displayed in the frequency change of the microbalance versus the exposure time t to the etching gas for a series of Cu(pure) film thicknesses D was carried out and a typical selection of results is collected in figure 6. The samples were transferred immediately after preparation to the etching cell and exposed to a gas
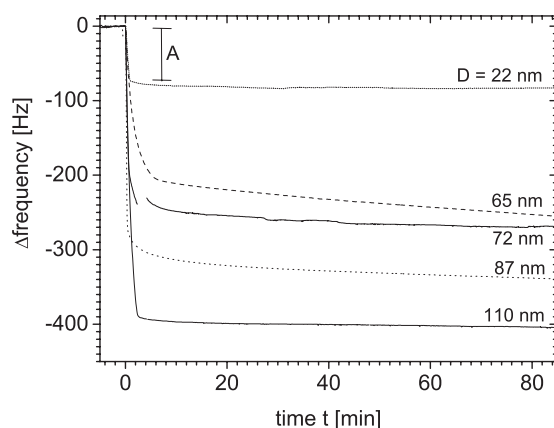
Figure 6. Dark reaction of Cu with Cl_2 for different films thicknesses D. Notice the extremely quick frequency change in region A at the beginning of the reaction.

flow of a mixture of Cl_2/Ar, $1:10^4$. The total pressure was stabilized by the flow controller to 0.2 mbar corresponding to a Cl_2 partial pressure of 2×10^{-5} mbar. The film thickness D and the rate $k(t)$ are recorded as frequency changes of the same microbalance and can therefore be directly related in terms of $CuCl_x$ if the different atomic weights of Cu and Cl are taken into account for x. The thickness in nm can be derived from equation (1) and the densities ρ. In addition the thickness reading was calibrated in a test experiment versus an AFM measurement leading to a value of 5.3 ± 0.3 Hz for $D = 1$ nm of Cu.

The results were unexpected in view of the available literature data [33, 34] and have therefore to be considered in more detail. Starting with the lowest thickness $D = 22$ nm we observe a very fast initial drop in A which is followed within a minute by a very slow decrease with an essentially constant rate. The transition from region A to the slow rate is very abrupt. One could assume that region A reflects processes at or near the surface which hinder a further reaction by a type of passivation. A very limited rate of diffusion into the bulk of the Cu film could also be responsible for this effect. In order to clarify this question the initial film thickness was increased systematically from $D = 22$ nm up to $D = 110$ nm. The data in figure 6 illustrate that the very same behaviour is observed for all values of D. In addition the initial fast frequency change in A in Hz increases proportionally to D. This linear correlation holds for a larger range of D according to figure 7. The slope can be directly expressed in terms of the frequency changes leading to D and the further increase in weight in step A due to the intake of Cl. The slope of A:$D = 0.62 \pm 0.05$ is close to the ratio of the atomic weights of Cl:Cu $= 35.85:63.55 = 0.56$. Thus figures 6 and 7 indicate that the complete Cu film reacts homogeneously within the first minutes to a $CuCl_x$ compound with $x = 0.9$. As regards the two relevant stoichiometries of CuCl and $CuCl_2$, obviously a strong preference for CuCl formation is observed. The first quick drop in A thus results from a homogeneous reaction of the Cu film essentially to CuCl. After completion of this stoichiometry the reaction rate decreases by two to three orders of magnitude for the formation of $CuCl_2$. The completion of $x = 0.9$ to 1 is buried in this transition and it cannot account alone for the further kinetics. After long exposure times the weight increase definitely requires $x > 1$; however a completion of the reaction in formation of $CuCl_2$ throughout the film would extend beyond the exposure times shown in figure 6.

These results revise expectations that one would draw from the literature data. Experiments with small exposures leading to coverages in the monolayer regime report a sticking coefficient
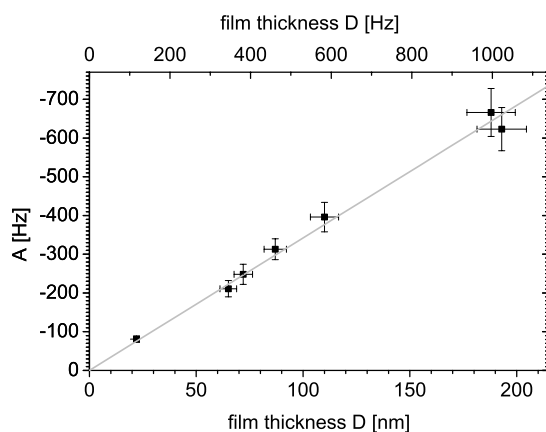
Figure 7. Frequency change of region A depending of the Cu film thickness D. The slope reflects the ratio of Cl:Cu.

initially near unity due to dissociative adsorption. After formation of a monolayer, passivation occurs and the sticking coefficient is reduced by orders of magnitude to values around 0.002 [35, 36]. Results for a single very thin film in figure 6 could have been misinterpreted in this way. The sequence of D values and the linear correlation in figure 7 prove however the homogeneous reaction. Our experiments correspond to a high exposure regime and are in this sense more similar to [33] and [34] where these passivation effects disappear. Besides this general similarity, our results disagree with those of [33] and [34] in two essential points. The Cl_2 partial pressures of the order of 10^{-4}–10^{-6} mbar correspond in view of [33, 34] to a low exposure regime. The initial rates in range A which we observe are however much larger than those reported there for similar exposures and they only show up for much higher exposures. The experiments in [33] were carried out with fixed exposure times of 50 s and therefore the dramatic change in the kinetics apparent in figure 6 could have been overlooked. In addition a gradual change in the distribution of CuCl and $CuCl_2$ with depth is reported in contrast to the initial homogeneous reaction seen in figure 7. These discrepancies have led us to a more detailed inspection of the rates in regime A.

For Cu(pure) films deposited purposely on unpolished quartz substrates exceptionally high rates of the order of 10^3 Hz min^{-1} were observed due to the roughness and the enlarged surface area. The initial rates in regime A of figure 6 for Cu(pure) on polished substrates were in the regime of 2–3×10^2 Hz min^{-1}. With increasing exposure to air, i.e. a transition to Cu(O) conditions, we observe a continuous and systematic decrease of this initial rate by one order of magnitude (10 min exposure to air) and even two orders of magnitude (62 days exposure to air). Thus contamination can lead to the behaviour seen in [33, 34]. Cu(O) will be discussed in the following section. For completeness we mention that our results are not influenced by artefacts due to the gas flow. We varied the gas flow for a constant total pressure and worked in the saturation regime with a reaction rate independent of flow to avoid a depletion of Cl_2 in the gas by the reaction. Furthermore we measured the dependence of the rate on total pressure for a constant dilution and found the expected proportional increase of the rate with pressure.

2.4. Dark reaction of Cu(O)

The influence of contamination on the reaction rates is illustrated in figure 8 for which the same exposure conditions as in figure 6 were used. Figure 8(a) repeats the curve for $D = 110$ nm
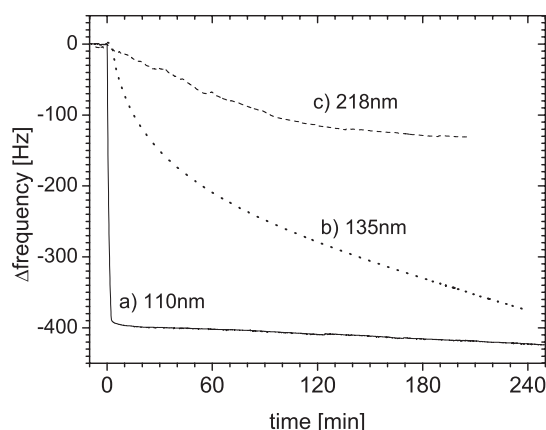
Figure 8. Dark reaction of three different prepared Cu films. Clean Cu film (a) with thickness 110 nm, also displayed in figure 7. Before evaporation the natural oxide was not removed from the Cu wires and therefore the oxide content is higher in film (b). Even more oxide is in film (c) which was in air for several weeks before the etch.

from figure 6 for comparison. The Cu film thickness $D = 135$ nm is displayed in figure 8(b) and the only significant change is that the oxide film on the Cu wire pieces was not mechanically removed before melting in the crucible. According to the trend in figure 6 it would be expected that curve (b) crosses curve (a) in Figure 8 within the first minutes and that it levels off around a value of -500 Hz. The slowing down of the reaction in (b) with respect to this expectation is astounding. The first fast part A from figure 6 is just absent and that means this immediate homogeneous reaction to CuCl is missing. This qualitative feature is most important and has to be kept in mind. If one were to take the rate df/dt let us say around 120 min in curve (b), it would exceed that in curve (a). However in curve (a) it was taken up already a chlorine amount corresponding to -400 Hz in the first minutes, while (b) is lagging far behind with a value around only -300 Hz after 120 min despite the larger thickness D which should drive the reaction to -500 Hz. Therefore the contaminated film in (b) is far away from the equilibrium that the pure film has reached long before and this lasting gradient obviously leads to the apparently larger rate df/dt at long times. The contamination is enhanced if such a film is exposed additionally to air for several weeks before etching and the reaction is slowed down even more according to figure 8(c). These delayed reactions like in figure 8(b) resemble the data in [33, 34] providing an explanation for the discrepancy.

We have to deal with these contaminated films more extensively because they are required for the light induced reactions which could not compete with the fast part A in figure 6. Furthermore the previous investigations with patterning of compact Cu plates revealed oxygen contamination and the results therefore belong also to this category. We took Auger spectra from reaction products on the evaporated films and they showed—besides of course Cl and Cu—also contributions from O and C. C most likely results from hydrocarbons involved in the cleaning procedure and pump oil. C from photodissociation or larger amounts of hydrocarbons can reduce light induced reactions [37]. Cu reacts however predominantly with oxygen [38] and OH and hydrocarbons interact with these films [39, 40]. Therefore we focus on the oxygen contribution. The enhancement of the delay with air exposure supports this assumption. The oxygen will be initially at the surface for the plates and the films with air exposure. For those contaminated during evaporation it is possible that oxygen floats on top in a surfactant type of behaviour [41].
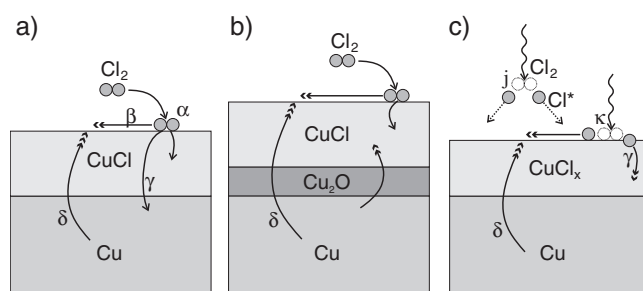
Figure 9. Scheme of dark reaction of Cl_2 with Cu(pure) (a) and Cu(O) (b). The faster the diffusion process, the greater the number of tips on the representing arrow. (c) Scheme of light induced reaction. Excitation of Cl_2 in the gas phase (j) leads to a non-selective reaction. Whereas a selective reaction takes place if adsorbed Cl_2 is excited (κ). For α, β, γ, δ, see the text.

In figure 9 we suggest three schemes which seem to summarize the available information. In the very first moments of a reaction unprotected Cu will be exposed to Cl_2 and the well known efficient dissociative chemisorption will take place [35, 36]. This process is completed already with formation of a monolayer and is not further relevant for the formation of product films in the range of 10 nm–10 μm considered here. On the passivating $CuCl_x$ layer Cl_2 molecules are physisorbed or chemisorbed (α) in figure 9(a). The barriers for lateral migration (β) of Cl_2 are smaller than those for penetrating into the bulk material (γ). Therefore delocalization on the surface is faster as visualized by the number of tips on the arrows and discussed in [15, 16]. The question is now whether the reaction proceeds via chlorine diffusion (γ) or Cu diffusion (δ). From the investigation of the composition of the films presented in section 3 it was concluded that $\delta > \gamma$ which is also in accordance with a more likely diffusion of Cu^+ or Cu^{2+} in an $CuCl_x$ ionic lattice compared to that of Cl^{2-} [42]. In this case the delivery of Cl via α is rate limiting, the dominance of δ with respect to γ leads to an abundance of Cu on top of the reaction product film and the large β allows us to bring the reaction partners together (figure 9(a)). Thus the Cu(pure) reactions of figure 6 will proceed by a diffusion of Cu through the film and a homogeneous conversion of all the available Cu (limited by D) to $CuCl_x$ occurs. $x = 1$, i.e. CuCl, prevails with respect to $x = 2$ due to the limitation of step α. An increase in Cl_2 pressure increases the rate in a linear way. As soon as process δ is terminated (step A in figure 6) by the consumption of the Cu reservoir (once more limited by D) only the transformation of $x = 1$ to 2 will continue to proceed. This requires chlorine diffusion with the lower diffusion rate γ which is reflected in the slow part of figure 6.

Now addition of the oxygen layer (figure 9(b)) still keeps the relation $\delta > \gamma$ according to section 3 and the film of reaction products grows on the surface thus burying the Cu(O) layer. However δ will be significantly reduced as displayed in figure 9(b) and expected from calculations of Cu diffusion in Cu_2O [43]. Binding of Cu atoms to oxygen enlarges the barrier for diffusion to 0.9 eV compared to 0.3 eV otherwise. Slowing down δ now gives room for partially shifting x to values above 1 in the initial reaction at the surface as well as some competing diffusion of chlorine via γ into the product film above the Cu_2O interlayer. Thus the composition of films like in figures 8(b) and (c) versus exposure should be studied in the future.

In the situation of reduced rates of figure 9(b) it becomes now feasible to stimulate the reaction with light. Dissociation of gas phase Cl_2 molecules j or adsorbed molecules κ by irradiation will lead to a more efficient adsorption of the reactive fragments. Dissociation of adsorbed molecules causes a faster reaction in the case of κ via a larger γ, β for the fragments.
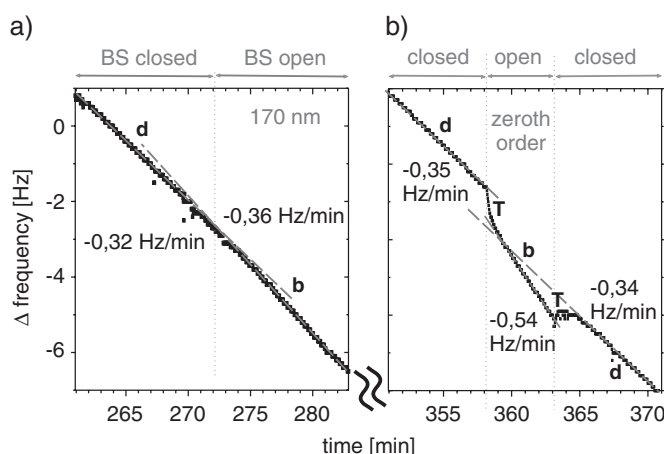
Figure 10. (a) Irradiating a Cu film with 170 nm induces a reaction which can be observed via a change of the rate (slope). The difference between the dark reaction as long as the beam shutter (BS) is closed (d) and the light induced reaction when the BS is open (b) is small. (b) The reaction is more obvious if the zeroth order of the monochromator is used. The change of frequency in the regions T is due to thermal effects.

Both processes result in a quicker depletion of Cu by the fragments and a faster diffusion via δ due to the disturbance of the chemical equilibrium. This situation illustrated in figure 9(c) leads to light induced reactions. In principle also the conversion of $x = 1$ to 2 in the slow part of figure 6 can be exploited for a light induced reaction based on the scheme of figure 9(a). Here, however, only the increase of γ will be possible and thus the efficiency is reduced. It is consistent with this picture that in section 3 a predominant $CuCl_2$ composition of the light induced reaction products will indeed be presented.

2.5. Light induced reaction of Cu(O)

In section 2.1 it has been pointed out that even for very efficient light induced reactions with $q_1 \approx 1$ the corresponding rates for Cl intake will be below 1 Hz min^{-1}. They have to be monitored in the presence of the dark reactions described in section 2.3. To verify that the sensitivity is high enough, irradiation with white light from the zeroth order of the grating is helpful because it provides the largest photon flux and no spectral regions are discriminated. The two parts 'd' at the beginning and end of figure 10(b) correspond to a dark reaction analogous to that of figure 8(b) after long exposure of 350 min to the same Cl_2/Ar mixture of 1:10^4 with 0.2 mbar total pressure, i.e. 2×10^{-5} mbar Cl_2 partial pressure. Consistently with figure 8 the dark reaction rate is small and slowly decaying from -0.35 to -0.34 Hz min^{-1} in a time interval of 20 min. The sample has been irradiated in the central part marked 'b' (for 'bright') with zeroth-order light. A quick drop is observed in the beginning of the light exposure which is reversed when the light is shut off at the end. Both changes are marked by 'T' in figure 10(b) and they correspond to the temperature changes addressed in figure 1(b), here caused by the light itself. In addition the reaction rate is enlarged in the central part of range 'b' in figure 10(b) to -0.54 Hz min^{-1}. The irradiation with zeroth-order light generates an additional rate of Cl intake corresponding to -0.2 Hz min^{-1}. The light irradiation lasted for 5 min and the Cl intake of 1 Hz is indeed irreversible. The slopes of the 'd' parts are very similar and extrapolation of the final part back to the initial part as indicated by the dashed line
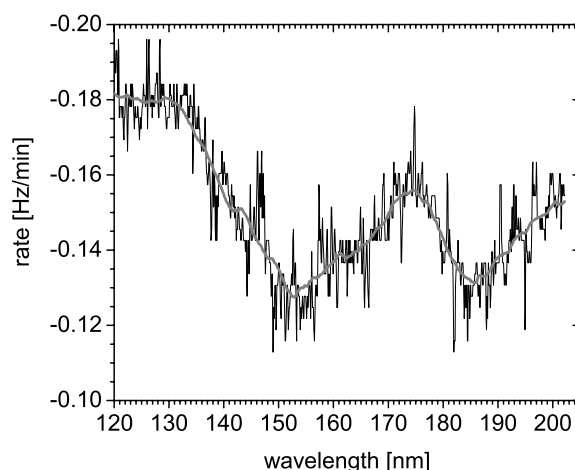
Figure 11. The rate displays the dependence of the reaction efficiency on the wavelength. The reaction is enhanced in the regions of 130, 170 and 200 nm.

delivers just this difference of 1 Hz due to the light induced reaction. Figure 10(b) gives a good impression of what one has to deal with.

Results for a similar experiment as regards Cl_2 exposure (2×10^{-5} mbar), however irradiating with wavelength dispersed light at a central wavelength of 175 nm, are shown in figure 10(a). The reaction rate increases now from -0.32 Hz min^{-1} in the initial dark reaction part 'd' to -0.36 Hz min^{-1} for the irradiated part 'b'. In this case the light induced rate corresponds to -0.04 Hz min^{-1}. The thermal effects disappear due to the lower photon flux. Optimizing for the light induced reaction allows one now to scan the wavelength and to determine the wavelength dependence of the light induced reaction rate. A scan velocity of the order of only 0.5 nm min^{-1} has to be chosen to provide a sufficiently long measuring time for each wavelength interval. The light induced reaction rate versus irradiation wavelength is depicted in figure 11 for the same Cl_2 exposure conditions (2×10^{-5} Cl_2 partial pressure) as in figures 8 and 10. The dark reaction contribution has been subtracted. The correction is subject to an uncertainty as has been illustrated; it is however a constant value with respect to the wavelength dependence. A significant light induced reaction is observed throughout the recorded wavelength range from 120 to 200 nm and on top of it three broad ranges of enhanced efficiency centred at 130, 170 and 200 nm can be discerned. They will be analysed in more detail in section 3 together with the results from light induced spatial patterns. Here we consider the value q_1 of reacted molecules per incident photon resulting from the frequency changes. Cl_2 molecules in the gas phase show strong absorption bands with vibrational structures in the range from 110 to 140 nm [44] and the absorption cross section drops by three orders of magnitude in the range from 140 to 200 nm. Therefore the Cl_2 gas in front of the substrate is transparent for the partial pressure employed in the long wavelength range in figure 11 and the band at 170 nm originates from a selective reaction due to excitation of the surface layers which will be proven also experimentally in section 3.2. The photon flux was recorded with a calibrated photodiode of 4×4 mm^2 area at the position of the sample, yielding a slight increase from 9×10^{11} γ s^{-1} for 130 nm to 1.1×10^{12} γ s^{-1} at 190 nm for a beam current of BESSY II of 100 mA h. The rates in figure 11 are normalized to 100 mA h and the active extent d_1 of the Cu spot of 2.8 mm is smaller than the diode extent, leading to an essentially wavelength independent photon flux on the active Cu area of 0.8×10^{11} γ s^{-1} or $N = 4.8 \times 10^{13}$ γ min^{-1}.

The measured frequency change $\Delta f_m = 0.16$ Hz min^{-1} in figure 11 at 170 nm is related to the number $N \cdot q_1$ of accumulated Cl atoms with $\Delta f = 3.23 \times 10^{-15}$ Hz from section 2.1 by

$$\Delta f_m = q_1 \cdot N \cdot \Delta f \tag{2}$$

and leads to $q_1 = 1.0 \pm 0.1$. The systematic errors for this quantum efficiency of unity due to the correction of the dark reaction background may exceed those from the photon flux and may become of the order of ± 0.5. The essential message is however that these light induced reactions occur with unexpectedly high quantum efficiencies compared to values of e.g. 7×10^{-4} from [45] for 10^{-4} mbar Cl_2 and 308 nm wavelength. The implications will be considered in section 3.

3. Light induced spatial product patterns on Cu(O)

Due to the lack of gas phase absorption it is natural to attribute the 170 nm band in figure 11 to a selective light induced reaction. It remains however to be clarified whether for the 130 nm wavelength region the selective or the non-selective contribution from excitation of Cl_2 gas dominates. In section 1 it has been explained that the efficient selective reaction reproduces the lateral spatial distribution of the irradiated light. In a non-selective reaction this spatial distribution will be washed out due to diffusion of the reactive gas phase species before starting the surface reaction. Using a mask in front of the substrate to generate a pattern of irradiated and dark structures and investigating the spatial distribution of the light induced products is therefore well suited for sorting out selective and non-selective contributions. The method allows for long accumulation times and the sensitivity can be increased even more by combining a high spatial resolution of the mask with a tight focusing of the irradiating light. The recorded quantity is the locally accumulated height of products which scales with the impinging number of photons per cm^2, while the frequency change Δf_m in equation (2) depends only on the overall flux on the quartz. The samples have however to be taken out of the chamber—after a predetermined exposure time—for evaluation. A continuous recording like in section 2 is not possible.

3.1. Product topography and depth profiles

In an etching cell similar to figure 2 the quartz substrate was replaced by polished high purity (above 99.99%) polycrystalline Cu plates with an extent of 16 mm along the direction of the dispersed light (figure 3). Polishing is necessary to reduce roughness and thus the dark reaction. For comparison the plates were replaced by a Cu(111) single crystal and the products were investigated *in situ* [15]. The method is illustrated in figure 12. The plate was covered with a Ni mesh used typically as a support in electron microscopy with a 10 μm width and 40 μm separation of the wires. The structure of this mask is well reproduced in the distribution of reaction products in the central irradiated part and leads to the contrast in the optical microscope picture of figure 12. This contrast reflects the selective contribution in the light induced reaction. Reaction products are also formed outside the irradiated spot; the contrast due to the mask is however fading away. An additional compact mask in the circumference of figure 12 protected these parts from any contact with light or etching gas and provides a reference for the original Cu surface. The light induced reaction was enhanced with respect to the dark reaction by exploiting the high photon flux in undispersed white light for a high beam current at BESSY I and the focusing leading to a larger number of photons cm^{-2}. A cross-check showed that the contribution of the dark reaction is negligible for these conditions (Cl_2 partial pressure of 10^{-3} mbar) and the products originate from light induced reaction inside and outside of the irradiated spot.
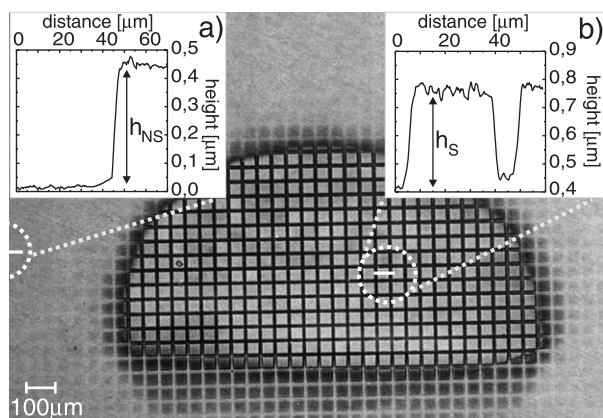
Figure 12. Optical microscope picture of a $CuCl_x$ film on a Cu sample which was exposed to 10^{-3} mbar Cl_2 and 1.5×10^{18} photons (zeroth order). Shaded areas appear dark. (a) AFM measurement showing the non-selective region with a step height h_{NS} of 0.45 μm. (b) The selective step height h_S of 0.38 μm was measured in the irradiated structured area of the focal spot.

The step height h_{NS} measured by an AFM from the original Cu surface to the top of the product film in the unirradiated part (figure 12(a)) corresponds therefore to the products from the non-selective reaction. If we move into the irradiated spot we find on top of these non-selective products a step height h_S (figure 12(b)) which corresponds to the selective reaction, in going from the minimum in the shaded parts (at the 10 μm wide wires) to the light exposed squares (40 μm wide). These step heights originate from the swelling due to the Cl intake in the $CuCl_x$ compound formation and thus the lower Cu density in the product film [15]. The Cu atoms have been removed from regions below the original surface, and distributed in the films. Therefore the product films extend also below the original surface and the real product heights are larger than h_S and h_{NS}.

The composition of similar product films versus depth was investigated with XPS (x-ray photoelectron spectroscopy) and SAM (scanning Auger microscopy) by sequentially removing product layers with Ar^+ ion sputtering. XPS has the advantage that it is sensitive to the chemical composition and allows one to distinguish between CuCl and $CuCl_2$ compounds via the shift in binding energies. Its large x-ray spot averages however with respect to the selective and non-selective parts. Before Ar^+ sputtering a larger content of CuCl (about a factor of 2) compared to $CuCl_2$ is found in the very top layer. This ratio is inverted in the bulk of the product film with predominant $CuCl_2$ and only about 20% of CuCl [15]. The scan range of only 500×500 nm^2 in the SAM measurements allowed us to take separate data from the selective and non-selective parts. SAM delivers however only the relative abundance of the atomic species and not the bonding character. The results are qualitatively similar for the different parts [15] and we show as an example the composition for a shaded area and strong irradiation in figure 13 which contains the essential features.

The depth profile can be divided into the top region A reflecting the reaction products, a transition region B and the onset of unreacted Cu bulk material in C. A shows an atomic ratio of Cu:Cl of 1:2 suggesting for these irradiation conditions a composition of predominantly $CuCl_2$. Near B the ratio changes to 1:1 (arrow) and in C it approaches continuously Cu bulk. In the B region also oxygen atoms appear from the O content on the original surface of the Cu plate. The O contamination is buried under the reaction products. Therefore the growth originates from a predominant diffusion δ of Cu atoms through the Cu_2O layer as indicated in figure 9. The
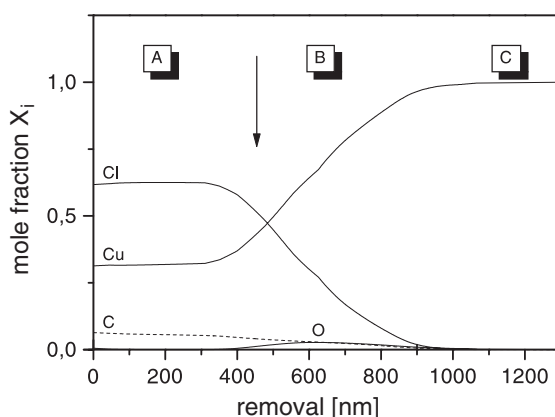
Figure 13. SAM depth profiles of shaded areas with Cl, Cu, C and O mole fractions after irradiation with white light. Region A is above, B below the original Cu surface (arrow). The composition of non-selective products below the shading mask can be concluded.

question remains of whether stimulation by light leads to a growth near the arrow in figure 13 or on top of the product film. A carbon tracer was introduced with a constant rate at a very low concentration. Its concentration is inversely proportional to the $CuCl_x$ growth rate. For a thick film the growth rate will slow down due to diffusion limitations. The increase in C concentration towards the surface indicates that the top parts were formed in the later stages of reaction. This C distribution shows that the light stimulated reaction proceeds on the actual surface of the reaction product film. The composition of the $CuCl_x$ product films which were irradiated with a smaller intensity shifts from $x = 2$ to smaller values between $1 \leqslant x \leqslant 2$ indicating a mixture of $CuCl_2$ and $CuCl$ with irradiation dependent ratio [15].

Combining the information in sections 2 and 3 leads us to the following rough scenario. The monolayer studies revealed a passivation by a CuCl monolayer allowing for adsorption of Cl_2 precursor molecules on the actual surface. For a pure Cu sample (figure 9(a)) these Cl_2 molecules are quickly consumed by fast diffusion δ of Cu and converted to CuCl. The passivating property of CuCl slows down the conversion to $CuCl_2$ by orders of magnitude (figure 6). Oxygen contamination now slows down Cu diffusion, delays the reaction (figure 8) and allows for a longer presence of the Cl_2 precursor on top of the CuCl passivation layer. The Cl_2 precursor reservoir is now amenable for a light stimulated reaction (figure 9(c)). Stimulation (figure 12) occurs via light absorption of molecules on the surface (selective process) or via activated species (Cl^* from dissociation or Cl_2^*) from the gas (non-selective process). It leads to a complete (figure 13) or partial conversion of the CuCl passivation layer to $CuCl_2$. The larger Cl intake causes the high rates in Δf and in step height measurements. An interesting question treated in section 3.2 concerns the efficiency in the activation–conversion sequence. It is also conceivable that the blocking property of Cu_2O is circumvented locally. A locally enhanced reaction is described indeed in [15] which leads to light induced volcano-like structures. They display a competition between surface and bulk diffusion processes which are however too complex to be treated here and call for further investigations.

3.2. Wavelength dependence and efficiencies

The etching cells with Cu plates were placed in analogy to figure 3 on a similar monochromator at BESSY I. The dispersion of the wavelength with 0.6 nm mm^{-1} across the samples (figure 4)
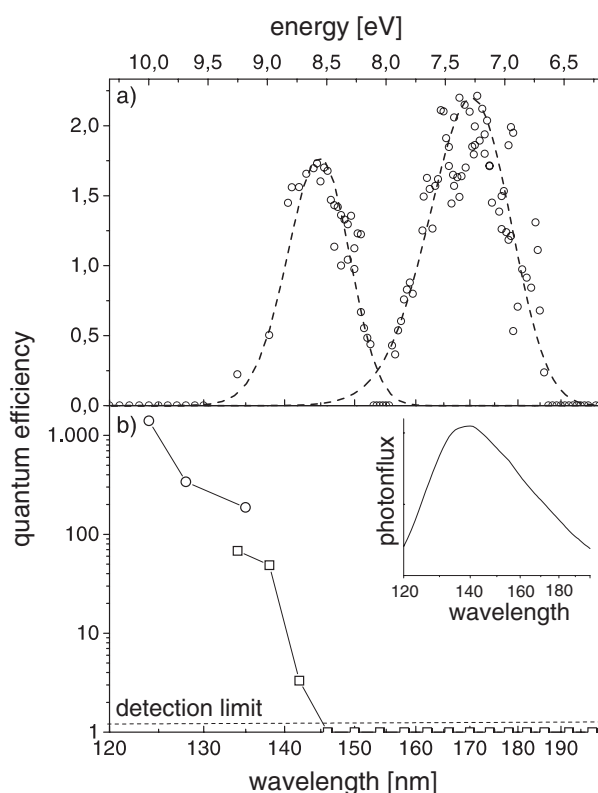
Figure 14. Quantum efficiency of the selective (a) and the non-selective reaction (b). The wavelength dependence of the photon flux is displayed in the inset.

with an extent of 16 mm corresponds to a spatially resolved recording of the wavelength dependence of the efficiency in an interval of $\Delta\lambda = 9$ nm. Repeating the experiments by translating the centre wavelength for otherwise identical conditions is demanding as regards the reproducibility of the procedure. It is however feasible [15] and delivers the efficiencies displayed in figure 14. The product step heights were determined by scanning with an AFM vertical to the direction of the dispersion. Non-selective and selective contributions can be separated in analogy to figure 12. Non-selective contributions were only observed for wavelengths shorter than 145 nm (figure 14).

The quantum efficiency q_1 of product formation per incident photon was derived for the selective reaction in figure 14(a) from the volume which corresponds to the measured step height and the number of photons cm^{-2}. A comparison of the strong band at 170 nm with the microbalance result in figure 11 confirms that this band is reproduced in both experiments and that it originates from a selective process. Also the absolute quantum efficiencies of $q_1 = 1$ in the microbalance data and of $q_1 = 2$ from the step height are quite consistent in view of the very different preparation conditions and the dependence on oxygen contamination. The bands were tentatively assigned to transitions in the adsorbed Cl_2 molecules allowing for red shifts and weakening of selection rules due to the interaction with the substrate [15]. Most striking are the q_1 values around unity. Certainly not every impinging photon will be absorbed in such a way as to generate an active centre on the surface. Since the overall efficiency q_1 is close to unity it is necessary that each active centre stimulates several Cl_2 molecules to a reaction. As

an illustration, suppose that the absorption cross section of an adsorbed molecule at 170 nm is very high and reaches 10^{-16} cm^2 and that also the coverage with adsorbed Cl$_2$ molecules is very high and reaches 1% of a monolayer or 10^{13} cm^{-2}. The absorption probability for these molecules is then 10^{-3}. To reach a value of unity for q_1 it is necessary that each of the excited molecules stimulates further 10^3 Cl$_2$ molecules to react and to convert for example 10^3 CuCl molecules to CuCl$_2$. This reaction efficiency which was named in the introduction q_2 corresponds in this example to $q_2 = 10^3$. While we are not yet able to derive a distinct value due to the lack of information on the microscopic details on the surface it is nevertheless clear that $q_2 \gg 1$ for the selective reaction at 170 nm. The band in figure 11 around 200 nm has not been found in figure 14(a). The decaying photon flux in this spectral region may have reduced the sensitivity too much in the step height experiments. The band at 150 nm in figure 14(a) is no longer resolved in figure 11 because it is covered by the strong non-selective band rising already at 145 nm in figure 14(b) which will be treated now.

The separation of selective and non-selective contributions is obviously an important advantage of the pattern method and it identifies the band around 130 nm as the onset of the non-selective process. The determination of q_1 for the non-selective reaction is more involved; this reaction is however very instructive as regards the q_2 value. The problem arises from the question of which fraction of photons impinging on the cell generates reactive Cl* or Cl$_2^*$ centres in the gas which reach the surface of either the plate in the pattern method or the Cu spot (d_1 in figure 4) of the microbalance. The crudest approximation takes all the photons on the entrance window and it leads to an order of magnitude underestimation of q_1. Starting with these lower limits for q_1 we arrive at 135 nm and a Cl$_2$ partial pressure around 10^{-5} mbar at $q_1 = 60$ for the patterning (figure 14(b)) and $q_1 = 0.2$ for the microbalance. The absorption cross section at 135 nm of Cl$_2$ averaged over the wavelength interval across the cell is 1×10^{-16} cm^2. The probability that a photon is absorbed in the Cl$_2$ gas on the 1 cm long path to the substrate is only 5×10^{-5} at the pressure employed. Thus an amplification with a q_2 value of 4×10^4 for the microbalance results or 1.2×10^6 for the pattern value has to be active. A more realistic estimate assumes that the active centres in the gas are distributed across the inner surface of the cell. This leads to a further enhancement by the ratio of cell surface to the probed surface which is 6 for the patterning and 280 for the microbalance geometry. Now we end up with a range of $q_2 = 1.1 \times 10^6$ for the microbalance and $q_2 = 7 \times 10^6$ for the pattern data. The consideration illustrates that mostly a variation of the geometric factors accounts for the different q_2 values from both methods. More important is the order of magnitude which demonstrates that one excited centre reaching the surface stimulates a reaction of further 10^6 Cl$_2$ molecules to convert CuCl to CuCl$_2$.

Thus both selective and non-selective reactions show a strong amplification effect in the q_2 values. An idea is presented in [15] as regards how the misfit of a CuCl$_2$ molecule in the passivating CuCl monolayer generated by the activated centre breaks up its structures. The lattice distortion allows further adsorbed but not excited Cl$_2$ molecules to attach and the reaction spreads out. The amplification requires also a fast surface diffusion of these adsorbed Cl$_2$ molecules to fuel the chain reaction. These diffusion properties are considered in some detail in [15] extending beyond the presentation here. It is however remarkable that a similar combination of passivation and amplification with large q_2 values shows up in the light induced desorption and thus dry etching of semiconductors with halogens is summarized in section 4.

4. Light induced desorption and patterning: XeF$_2$/Si(100) and Cl$_2$/GaAs(100)

In this section we deal with combinations of substrates and halogens for which a part or all of the various light induced reaction products are volatile. The volatile products desorb and
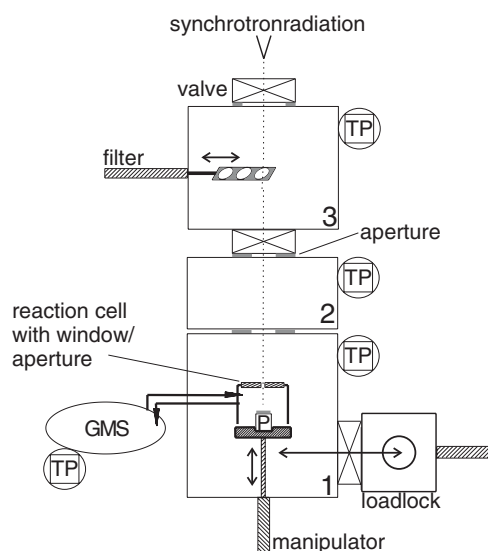
Figure 15. Scheme of the etching set-up with three pressure stages. Gases are mixed in the gas mixing chamber (GMS).

we arrive at the very heart of this Special Issue. This light induced desorption in reaction cells with a mask like in section 3.2 will occur preferentially in the irradiated parts and the structure of the mask can be imprinted directly in the substrate. This so-called 'dry etching' process is an interesting method for microstructuring of surfaces and for reproduction of mask structures. The wavelength range of 200–50 nm investigated here is especially relevant since it follows the mainstream, documented for example in the International Technology Roadmaps for Semiconductors (see footnote 1) which demands evolution from the UV spectral range into the VUV spectral range in order to relax the diffraction limitations. To eliminate the constraint imposed by the onset of absorption in the entrance window (113 nm for MgF_2, 105 nm for LiF_2) of the etching cell a modification as shown in figure 15 has been introduced. The entrance window is replaced by an aperture and a sequence of three pressure stages which reduce a pressure of 0.1 mbar in the cell to 10^{-9} mbar in the attached monochromator. The reduction is necessary to protect its optics from the aggressive halogen gas.

In general a mixture of volatile and non-volatile reaction products can be expected and its composition can depend on irradiation wavelength and exposure conditions. In this case a film from the non-volatile products is going to develop on the surface which is rather fluffy due to the volatile products escaping through it. These dust-like films have been observed for specific irradiation conditions of GaAs and Cl_2 [24] and it was shown that they can be removed easily for example by flashing with an excimer laser. In the following we restrict ourselves to the more generic case of complete desorption of the reaction products.

Si and GaAs substrates were chosen in order to deliver results for the two most prominent members of the family of semiconductors. They were used in the form of standard, single-crystalline wafer material with (100) orientation and n-type doping. The etching gases Cl_2 and XeF_2 result from a search for high efficiency which is motivated scientifically for studying a generic process and from the point of view of application it represents an efficient use of expensive photons. The white powder XeF_2 with a high vapour pressure is a convenient replacement for the more difficult to handle F_2 gas.

The efficient desorption simplifies the situation with respect to sections 2 and 3 because the complications due to the required diffusion of material through the capping product layer are obsolete. It means however also a loss of information since the composition of the products is not available for characterizing the reaction. The identified efficient etching gas/substrate combinations have several basic features in common with the Cu/Cl_2 system. The chemical equilibrium favours the products and a strong dark reaction leading to a quick and complete consumption of the substrate could be expected. The reaction is once more slowed down by a passivating top layer. In the GaAs case it is a GaCl layer on top of which adsorbed Cl_2 molecules float [24]. They represent the reservoir to be stimulated by light for a reaction. A fluorosilyl layer with a tree-like structure of Si–F bonds plays this role in the Si case [18]. Efficient light induced etching requires gas pressures of XeF_2 and Cl_2 of the order of 10^{-2} and 1 mbar respectively. The increase in gas pressure by three to five orders of magnitude compared to the Cu/Cl_2 case enhances the probability for gas phase absorption from a range of 10^{-5} up to 10^{-2} and even to unity. Therefore the balance of selective and non-selective reactions has to be considered first.

4.1. Wavelength dependence of selective and non-selective etching

Control experiments showed that the dark reaction contributions are negligible for the exposure conditions employed in the following and it is sufficient to consider the competition of the selective and non-selective light induced processes. Results for a wavelength dispersed etching of a Si sample analogous to that of figure 4 with a piece of wafer replacing the quartz are shown in figure 16. An interference microscope picture with a magnification of 400 in figure 16(a) shows the replica of the mask which is etched into the wafer. The top parts of the grid represent those areas which were protected by the wires of the mask. In this example the spectral range from 136 to 142 nm was dispersed across the wafer piece. Taking a scan with a stylus perpendicular to the direction of dispersion for the position of $\lambda = 137$ nm leads to the comb structure displayed in figure 16(b). The depth distribution reflects the intensity distribution in the focal line which originates from the intensity distribution along the entrance slit. The needles display the cuts through the grid in figure 16(a) and they all reach up to the original surface which shows up in the non-irradiated boundary regions. Moving now on the same wafer piece by 5 mm leads us to the position of a wavelength $\lambda = 140$ nm and a similar stylus cut results in the comb structure of figure 16(c). The basic features are similar to those in figure 16(b); the top of the needles remains however below the original surface as indicated by d_{US}. Obviously the protection by the mask wires was incomplete in figure 16(c) and the missing part d_{US} results from non-selective etching while the remaining needle height d_S displays the competing selective etching process. The comparison of figures 16(b) and (c) demonstrates why selective processes have to be preferred for a high quality reproduction of masks and it indicates the way in which both process efficiencies can be quantified. The wavelength dependence of the non-selective contribution in figure 17(a) is related to the absorption spectrum [46] of XeF_2 in figure 17(b). The maxima in non-selective etching efficiency follow those in absorption.

The absorption of XeF_2 consists of a broad maximum around 158 nm due to valence excitations and several progressions of sharp Rydberg transitions at shorter wavelengths. XeF_2 dissociates in this spectral range with high efficiency to XeF and F [46]. Fragments from the dissociation migrate by diffusion to parts below the mask and cause the non-selective etching.

Relevant for microstructuring are the minima in figure 17 because there the selective etching will not be distorted; it should have however a large efficiency by itself. The wavelength dependence of the selective etching efficiency in figure 18(a) shows that both conditions can be fulfilled for specific wavelengths in the range from 112 to 120 nm [20].
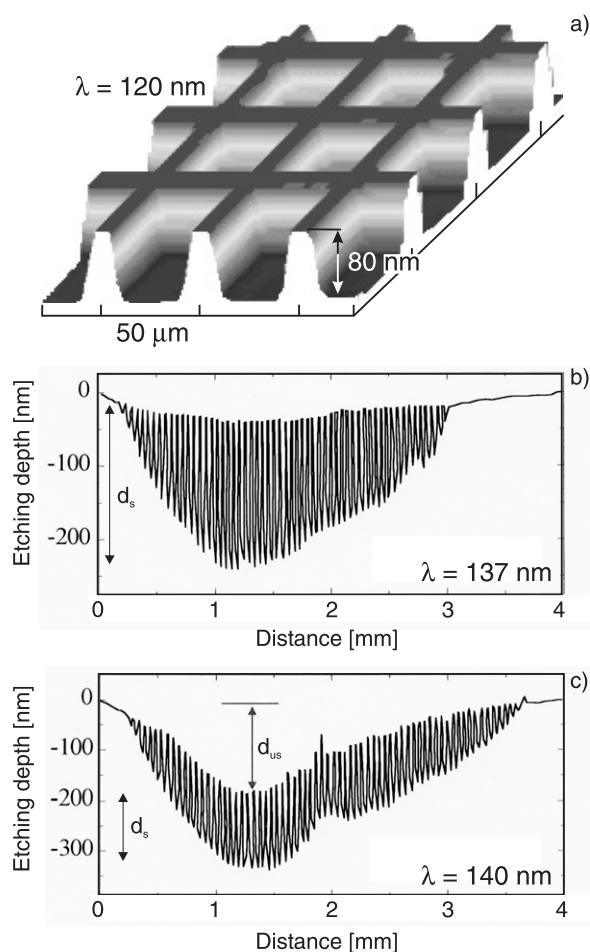
Figure 16. Etching of Si with XeF$_2$ produces good structures. (a) AFM picture of a sample irradiated with 120 nm. The distance of the grids, which were covered by a mask is 50 μm. (b) Cross section measured with a stylus of an irradiated area, which was covered by a mask. Only a selective reaction is observed (d_s) for $\lambda = 137$ nm. (c) Irradiating with 140 nm induces selective (d_s) and non-selective reactions (d_{us}).

A similar set of data for the etching of GaAs with Cl$_2$ deliver a simpler situation as regards both processes [24]. The gas phase excitation does not lead to etching and thus the non-selective process is so inefficient that it need not be considered in the interesting spectral range of 200–100 nm. Selective etching starts for wavelengths around 135 nm and it becomes very prominent between 115 and 130 nm according to figure 18(b). The minima between 120 and 130 nm originate from strong Cl$_2$ gas phase absorptions and the Cl$_2$ gas in front of the sample acts as a filter. The gas phase excitation does not contribute to etching and the surface is not reached by the light.

4.2. Etching efficiency q_1, amplification q_2 and pitch size

The quantum efficiencies q_1 of removed Si atoms or GaAs units per photon incident in the cell have been determined from the number of photons cm^{-2} and the etched volume analogous to
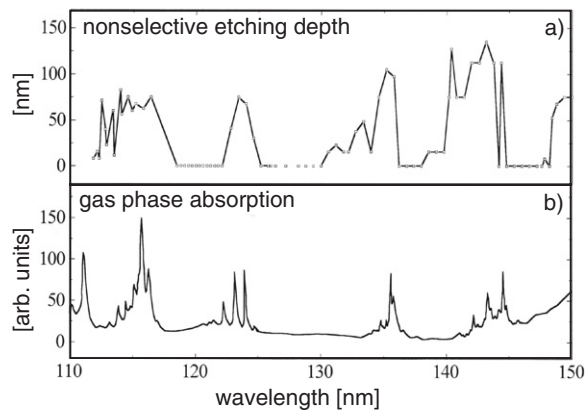
Figure 17. Correlation between gas phase absorption and etching efficiency in the case of Si/XeF$_2$. (a) Dependence of non-selective etching depth on the irradiated wavelength. (b) Gas phase absorption spectra of XeF$_2$ [46].
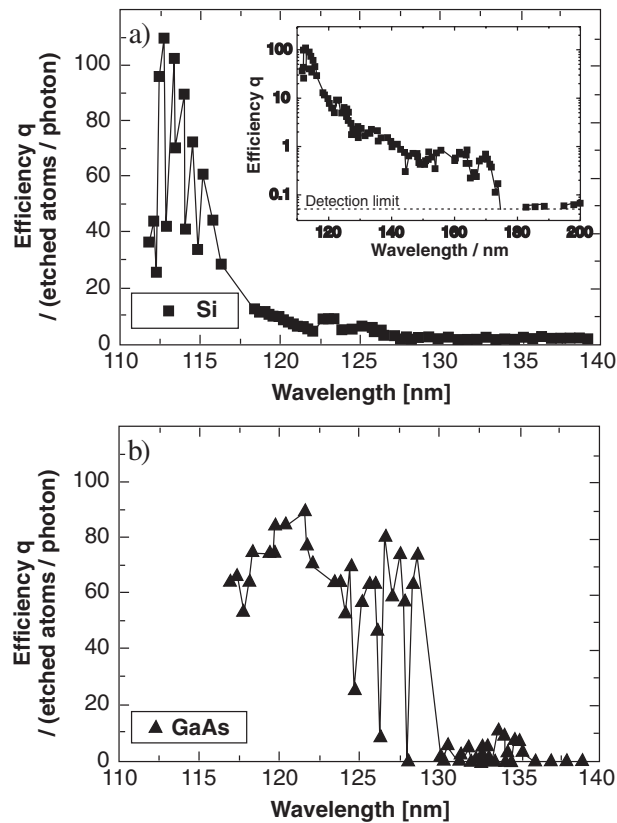

Figure 18. (a) Selective etching efficiency of Si/XeF$_2$. (b) Etching efficiency of GaAs with Cl$_2$.

that of section 3.2 and are shown in figure 18. They are once more much larger than unity and reach values in the range of high efficiency between 60 to 80 for GaAs [24] and up to 100 for Si [21]. Since they exceed unity it is necessary per se that amplification processes as discussed
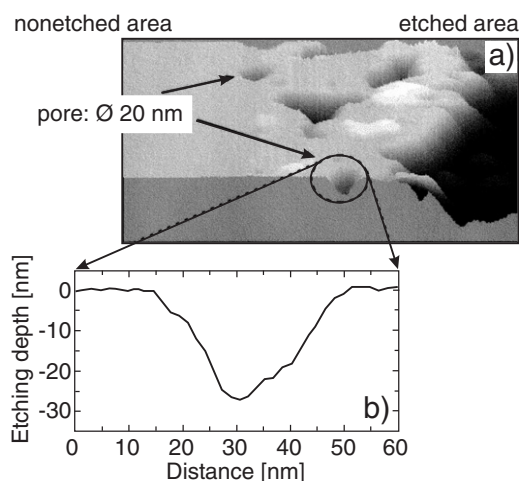
Figure 19. Si pore at the border between etched and non-etched areas resulting from a single-photon event. AFM cross sections show that the pore has a diameter of 20 nm and corresponds to about 3×10^5 Si atoms.

in the Cu/Cl$_2$ case are present also here. An excitation of the Cl$_2$ precursor molecules on the passivated GaCl layer has been identified as the initiating step [24]. A consideration analogous to that of section 3.2 leads once more to a very low absorption probability for these precursors and thus an amplification with estimated values of $q_2 = 10^5$ had to be postulated [24].

The volume corresponding to such large q_2 values is of the order of 10^3 nm^3. If this volume is for example distributed over a single layer, then the large extent with a diameter of the order of 200 nm would cause difficulties for identifying such a single-photon event. A concentration in a ball-like structure would lead to diameters of a pitch from a single reaction chain of the order of some 10 nm and a similar depth. Such a structure could be separated from smaller steps due to inhomogeneities on the surface. Inspection of the transition area between etched and shaded parts in Si/XeF$_2$ indeed revealed these pitches with a density distribution as expected from the light intensity distribution [18] in SEM (scanning electron microscopy) pictures. The pitch size appeared also as a roughness in those parts which where etched much deeper than a single pitch diameter. With this background information it was possible to analyse quantitatively the three-dimensional pitch structures resulting from individual single-photon events in AFM profiles [23]. The diameter of such pores of 20 nm and the depth profile shown in figure 19 indeed results in 3×10^5 atoms which were removed in a single pitch. These results deliver a direct measurement of the efficiency q_2 in the amplification processes. Since these high q_2 values are settled experimentally it remains to treat the microscopic processes in more detail. Density functional calculations seem to have the potential for proceeding in this direction [47].

4.3. Pitch structure and pattern quality

The amplification factor q_2 pays off by multiplying the efficiency of photons in consideration for microstructuring application. The large q_2 values demonstrated in sections 3.2 and 4.2 are indeed very promising in this sense. The pitch geometry shown in figure 19—while it is helpful for quantitatively pinning down the value of q_2—has a disadvantage as regards the quality of a pattern reproduced in this way. The roughness apparent in all dimensions reduces the fidelity and limits the achievable spatial resolution. Manipulation of the pitch
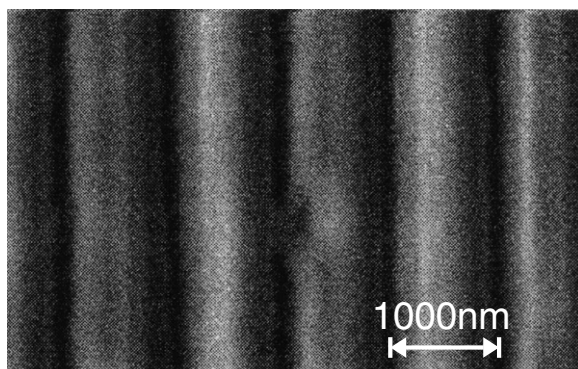
Figure 20. GaAs etched with Cl_2. The stripes are 1000 nm apart.

size by changing pressure and adding additional gases like O_2 has been demonstrated [18]. In particular SEM pictures of etched GaAs wafers revealed very smooth surfaces. A study devoted to the achievable spatial resolution showed that the structures are indeed only limited by diffraction [25]. Thus the combination of GaAs and Cl_2 seems to be very promising for proceeding further in this direction. As an illustration we show in figure 20 an SEM picture of a structure etched into GaAs as described above however with a much finer mask structure and a periodicity of 1000 nm. The resolution of the instrument was not high enough to provide a contrast quality which would be desirable. It is however sufficient to prove that the lateral width of the etched wall is 100 nm or even less, in agreement with the diffraction limit.

Acknowledgments

References

[1] Petek H and Ogawa S 1997 *Prog. Surf. Sci.* **56** 239
[2] Frischkorn C 2005 *Surf. Sci.* **593** 67
[3] Moresco F 2004 *Phys. Rep.* **399** 179
[4] Bartels L, Wang F, Moller D, Knoesel E and Heinz T F 2004 *Science* **305** 648
[5] Bäuerle D 1996 *Laser Processing and Chemistry* 2nd edn (Berlin: Springer)
[6] Tenhaile B R, Antonov V N, Xu G J, Nakayama K S and Weaver J H 2005 *Surf. Sci.* **583** L135
[7] Rosei F 2004 *J. Phys.: Condens. Matter* **16** S1373
[8] Hayasaka N, Hiraya A and Shobatake K 1987 *Japan. J. Appl. Phys.* **26** L.1110
[9] Nonogaki Y, Katoh M, Matsushita K, Suzui M and Urisu T 2005 *J. Electron Spectrosc. Relat. Phenom.* **144–147** 1113
[10] Bahrdt J and Schwentner N 1983 *Nucl. Instrum. Methods* **216** 237
     Bahrdt J, Gürtler P and Schwentner N 1987 *J. Chem. Phys.* **86** 6108
[11] Li B, Twesten I and Schwentner N 1993 *Appl. Phys.* A **56** 355
[12] Streller U, Krabbe A and Schwentner N 1997 *Appl. Surf. Sci.* **109/110** 442
[13] Raaf H and Schwentner N 1999 *Appl. Surf. Sci.* **138/139** 271
[14] Raaf H, Groen M and Schwentner N 2000 *Appl. Surf. Sci.* **154/155** 536
[15] Raaf H and Schwentner N 2001 *Appl. Surf. Sci.* **174** 13

[16] Ney V 2004 Lichtinduziertes Trockenätzen von Kupfer und Kobalt mit Chlor *Dissertation* Freie Universität Berlin
[17] Li B, Streller U, Krause H-P, Twesten I and Schwentner N 1995 *J. Appl. Phys.* **77** 350
[18] Streller U, Li B, Krause H-P and Schwentner N 1996 *J. Vac. Sci. Technol.* B **14** 91
[19] Streller U, Li B, Krabbe A and Schwentner N 1996 *Appl. Surf. Sci.* **96–98** 448
[20] Streller U, Krabbe A and Schwentner N 1996 *Appl. Surf. Sci.* **106** 341
[21] Streller U, Krabbe A and Schwentner N 1996 *Appl. Phys. Lett.* **69** 3004
[22] Streller U, Krabbe A, Raaf H and Schwentner N 1998 *Superlatt. Microstruct.* **23** 445
[23] Streller U, Raaf H and Schwentner N 1998 *Proc. SPIE* **3274** 112
[24] Li B, Twesten I and Schwentner N 1993 *Appl. Phys.* A **56** 355
[25] Li B, Twesten I, Krause H-P and Schwentner N 1994 *Appl. Phys. Lett.* **64** 1635
[26] Li B, Streller U, Krause H-P, Twesten I, Schwentner N, Stepanenko V and Poltoratskii Y 1995 *Appl. Surf. Sci.* **86** 577
[27] Dobrotvorskaya M V, Stepanenko V, Streller U, Raaf H and Schwentner N 1998 *Appl. Surf. Sci.* **136** 331
[28] Dietz V and Schwentner N 2003 *Surf. Sci.* **528** 215
[29] Soares D M, Wasle S, Doblhofer K and Tenan M A 2002 *Chem. Phys. Chem.* **9** 817
[30] Delval C and Rossi M J 2004 *Chem. Phys. Chem.* **6** 4665
[31] Hayderer G, Schmid M, Varga P and Aumayr F 1999 *Rev. Sci. Instrum.* **70** 3696
[32] Sauerbrei G 1959 *Z. Phys.* **155** 206
[33] Sesselmann W and Chuang T J 1986 *Surf. Sci.* **176** 32
[34] Sesselmann W and Chuang T J 1986 *Surf. Sci.* **176** 67
[35] Goddard P J and Lambert R M 1977 *Surf. Sci.* **67** 180
[36] Westphal D and Goldmann A 1983 *Surf. Sci.* **131** 92
[37] Li B 1992 Photochemical Reaction of Cu and GaAs with Cl$_2$ in the VUV *Dissertation* Freie Universität Berlin
[38] Chawla S K, Rickett B I, Sankarraman N and Payer J H 1992 *Corros. Sci.* **33** 1617
[39] Bojko I, Hilleret N and Scheuerlein C 2000 *J. Vac. Sci. Technol.* A **18** 972
[40] Haugsrud R 2002 *J. Electrochem. Soc.* **149** B14
[41] Steigerwald D A, Jacob I and Egelhoff W F Jr 1988 *Surf. Sci.* **202** 472
     Egelhoff W F Jr and Steigerwald D A 1989 *J. Vac. Sci. Technol.* A **7** 2167
[42] Walter W, Maolopoulos D and Jones R 1996 *Surf. Sci.* **348** 115
[43] Wright A F and Nelson J S 2002 *J. Appl. Phys.* **92** 5849
[44] Lee L C, Suto M and Tang K 1986 *J. Chem. Phys.* **84** 5277
[45] van Veen G, Baller T and Dieleman J 1988 *Appl. Phys.* **47** 183
[46] Nielsen U and Schwarz W H E 1976 *Chem. Phys.* **13** 195
     Black G, Sharpless R L, Lorents D C, Huestis D L, Gutscheck R A, Bonifield T D, Helms D A and Walters G K 1981 *J. Chem. Phys.* **75** 4840
     Kono M and Shobatake K 1995 *J. Chem. Phys.* **102** 5966
[47] Jenichen A and Engler C 2001 *Surf. Sci.* **475** 131